

# CXOCY J220132.8-320144: AN EDEG-ON SPIRAL GRAVITATIONAL LENS<sup>1,2</sup>

FRANCISCO J. CASTANDER<sup>3,4</sup>, EZEQUIEL TREISTER<sup>5,6,7</sup>, JOSÉ MAZA<sup>5</sup> AND ERIC GAWISER<sup>6,7,8</sup>

*In press*

## ABSTRACT

We present the CXOCY J220132.8-320144 system, which is composed of an edge-on spiral galaxy at  $z = 0.32$  lensing a  $z = 3.9$  background quasar. Two images of the quasar are seen. The geometry of the system is favorable to separate the relative mass contribution of the disk and halo in the inner parts of the galaxy. We model the system with one elliptical mass component with the same ellipticity as the light distribution and manage to reproduce the quasar image positions and fluxes. We also model the system with two mass components, disk and halo. Again, we manage to reproduce the quasar image positions and fluxes. However, all models predict at least a third visible image close to the disk that is not seen in our images. We speculate that this is most likely due to extinction by the disk. We also measure the rotational velocity of the galaxy at 2.7 disk scale radius to be  $v_c = 130 \pm 20$  km s<sup>-1</sup> from the [OII] emission lines. When adding the rotational velocity constraint to the models, we find that the contribution to the rotational velocity of the disk is likely to be equal to or larger than the contribution of the halo at this radius. The detection of the third image and a more accurate measurement of the rotational velocity would help to set tighter constraints on the mass distribution of this edge-on spiral galaxy.

*Subject headings:* dark matter — galaxies: spiral, structure, halos – gravitational lensing

## 1. INTRODUCTION

The current picture of galaxies is that they are composed of baryons (stars, gas, dust) and non baryonic dark matter. While observationally the distribution of the baryons can be studied, it is difficult to probe how the dark matter is distributed compared to the baryons. Traditionally, the study of galaxy dynamics has been the strongest proof of the existence of dark matter in galaxies (e.g., Rubin & Ford 1970; Faber & Gallagher 1979; Rubin et al. 1985). But given the inherent degeneracies in the inversion of dynamical data to obtain density profiles, it is hard to measure how the dark matter is distributed.

Another approach is to use gravitational lens systems. For strongly lensed quasars (QSOs), the geometry and photometric properties of the lens system depend on the projected mass inside the lensed QSO images and therefore can be used to constrain the mass distribution.

For the particular case of spiral galaxies, generally composed of a bulge, a disk and a dark matter halo, the rotational velocity curves cannot disentangle the relative contributions of the different mass components in the inner (luminous) parts of the galaxy. On the other hand, gravitational lenses offer the possibility of doing

so, especially in the case of edge-on spirals.

There are only five spiral gravitational lenses known so far (B0218+357: Patnaik et al. 1993; PKS 1830-211: Pramesh Rao & Subrahmanyam 1988; Q2237+0305: Huchra et al. 1985; B1600+434: Jackson et al. 1995; PMN J2004-1349: Winn et al. 2001). Only one of them is seen edge-on, B1600+434. However, none of them is ideal for studying the relative mass contribution of the different components.

Here, we report the discovery of an edge-on spiral lens galaxy as part of the CYDER survey, which may be the best spiral lens system to separate the relative mass contributions of its constituents. The Calán-Yale Deep Extragalactic Research (CYDER) survey (Castander et al. 2003b; Treister et al. 2005, hereafter T05) is an optical and near-infrared imaging and spectroscopic program carried out in archived, moderately deep *Chandra* fields. CXOCY J220132.8-320144 (hereafter CY 2201-3201) is one of the faint X-ray sources detected by CYDER in its D1 field. Optical follow-up of this field seemed to suggest that CY 2201-3201 was an edge-on spiral with a very bright nucleus. However, optical spectroscopy and imaging of this source in good seeing conditions revealed its true nature. CY 2201-3201 is a lensing system, showing two images of a distant  $z = 3.9$  quasar being lensed by an edge-on spiral galaxy at  $z = 0.32$ .

The paper is structured as follows. In §2 we present in chronological order the observational data gathered to characterize this system. In §3 we analyze the observational constraints obtained, and discuss them in §4. Finally we draw our conclusions in §5. Throughout, we assume  $\Omega_o = 0.3$ ,  $\Omega_\Lambda = 0.7$  and  $H_o = 70h_{70}$  km s<sup>-1</sup> Mpc<sup>-1</sup>.

## 2. OBSERVATIONS

### 2.1. X-Rays

CY 2201-32 was observed by the *Chandra* X-Ray Observatory with the ACIS-I instrument for 50.16 ks in 2000

arXiv:astro-ph/0611330v1 10 Nov 2006

<sup>1</sup> Partly based on observations collected at the European Southern Observatory, Chile, under programs 72.A-509 and 74.A-0493

<sup>2</sup> This paper includes data gathered with the 6.5 meter Magellan telescope located at Las Campanas Observatory, Chile

<sup>3</sup> Institut d'Estudis Espacials de Catalunya, Campus UAB, 08193 Bellaterra, Barcelona, Spain

<sup>4</sup> Institut de Ciències de l'Espai/Consejo Superior de Investigaciones Científicas (CSIC), Campus UAB, 08193 Bellaterra, Barcelona, Spain

<sup>5</sup> Departamento de Astronomía, Universidad de Chile, Casilla 36-D, Santiago, Chile

<sup>6</sup> Department of Astronomy, Yale University, P.O. Box 208101, New Haven, CT 06520

<sup>7</sup> Yale Center for Astronomy and Astrophysics, Yale University, P.O. Box 208121, New Haven, CT 06520

<sup>8</sup> National Science Foundation Astronomy and Astrophysics Postdoctoral Fellow

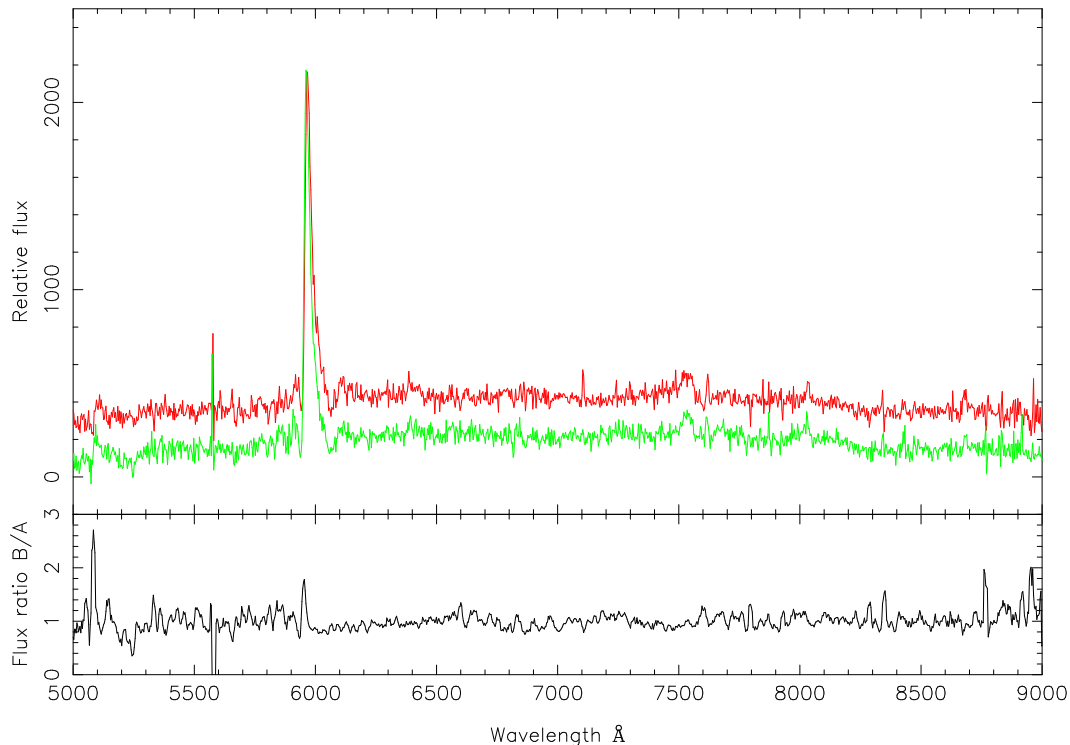


FIG. 1.— *Top*: VLT extracted spectra of image A (*upperline*) and B (*lowerline*) of the  $z=3.90$  lensed QSO. For displaying purposes the spectrum of component A has been shifted vertically. *Bottom*: Flux ratio of the two component spectra. In order to avoid contamination from the other QSO spectrum, both QSO components extraction apertures are narrow. Notice the small difference in apparent redshift due to a slit width considerably wider than the seeing and the two images not being aligned along the slit. This observational configuration makes each image of the QSO go through a slightly different part of the grism and therefore the same wavelength is not at the same pixel position.

July as part of the observation of the HCG90 field (PI Bothum). We retrieved this image from the archive and analyzed it using standard techniques with the CIAO package (Castander et al. 2003a, T05).

CY 2201-32 was detected in the soft band (0.5-2.0 keV) with  $11.6 \pm 3.9$  counts and undetected in the hard band (2.0-8.0 keV). We computed an X-ray flux of  $f_x = 1.06 \times 10^{-15}$  erg cm $^{-2}$  s $^{-1}$  and X-ray luminosity of  $L_x = 1.49 \times 10^{44}$  erg s $^{-1}$  in the soft band (T05).

## 2.2. CTIO Optical

As part of the CYDER survey we imaged the CYDER D1 field (T05) with the Cerro Tololo Inter-American Observatory (CTIO) 4m telescope using the Mosaic II camera in 2001 August. We took images for a total of 6600 and 1800s in the  $V$  and  $I$  bands, reaching limiting magnitudes of  $V = 26.7$  and  $I = 25.1$  and effective seeings of  $1.0''$  and  $0.9''$ , respectively.

CY 2201-3201 appears in these CTIO images as an edge-on spiral with a very bright nucleus/bulge with a total measured magnitude of  $V_{Vega} = 21.26$  and  $I_{Vega} = 19.94$ .<sup>9</sup>

## 2.3. VLT Spectroscopy

On 2003 October 31, we took spectra of the X-ray optical counterparts in the CYDER D1 field with the UT4 VLT FORS2 instrument. We used the 300V grism which

<sup>9</sup> Note that these magnitudes differ from the ones reported in Treister et al. (2005). The magnitudes presented here are total magnitudes while those of Treister et al. (2005) are aperture magnitudes with a relatively small aperture missing considerable amounts of flux for this extended source.

gives a resolution of  $R \sim 520$  ( $10.5 \text{ \AA}$ ) for our  $1''$  slits. CY2201-3201 was observed in one of our masks. Given the multi-object purpose of the masks, all slits were oriented north-south. We took five exposures of 1800 s in seeing condition of  $0.50''$ - $0.75''$  and bright/grey sky conditions. We reduced the spectra using standard IRAF<sup>10</sup> routines. Surprisingly, for this source we found two spectra of a QSO at a redshift of  $z=3.90$  in our best seeing spectra (see Fig. 1). The two QSO spectra were blended in our worse seeing exposures. Our 30 s mask acquisition image taken with a seeing of  $0.45''$  confirmed the existence of two point sources close to the center of the edge-on spiral galaxy, and therefore confirmed the lensing nature of the system.

## 2.4. Magellan Optical Imaging

We observed the CY 2201-3201 system with the Magellan Clay telescope using the MagIC instrument on 2004 September 8. MagIC has a pixel scale of  $0.0691''$  pixel $^{-1}$ . We took a series of 300 s exposures in three filters (SDSS  $g$ ,  $r$  and  $i$ ) for a total of 1800, 2400, and 1800 s in the  $g$ ,  $r$  and  $i$  filters respectively.

We reduced the images using standard procedures in IRAF. The resulting combined images have effective seeings of  $0.68''$ ,  $0.65''$  and  $0.62''$  in  $g$ ,  $r$ , and  $i$ , respectively.

Figure 2 shows the combined  $i$ -band image. The system configuration is composed of an edge-on spiral with two images of the QSO at each side of the disk. This is one of the expected configurations produced by an edge-

<sup>10</sup> IRAF is distributed by the National Optical Astronomy Observatory which is operated by AURA Inc. under contract with the NSF.

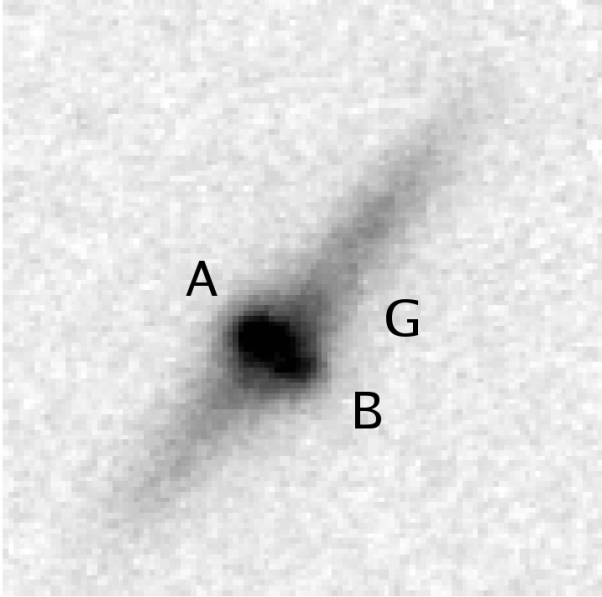


FIG. 2.— Magellan MagIC *i*-band image of CY 2201-3201. Image size is  $8'' \times 8''$ . North is up and east is to the left. The QSO images are marked A and B, and the galaxy G.

on spiral galaxy lens (Keeton & Kochanek 1998), except that it is missing a third image that should be located close to the disk.

To obtain tight constraints in the lens modeling it is important to know as accurately as possible the position and the fluxes of the observed components. In our images the seeing is only slightly smaller than the QSO images separation. Therefore the overlap between the QSO images and the galaxy light distribution makes it hard to separate their relative fluxes and determine their positions. We have thus used a Monte Carlo Markov Chain method (MCMC; Metropolis 1953; Hastings 1970, Gilks et al. 1996) to try to determine the positions and fluxes (and their errors) of the three components as accurately as possible.

We model the system with three components, two point sources (QSO\_A and QSO\_B) and a spiral galaxy. Each point source is modeled with three parameters: the  $\alpha$  and  $\delta$  of its center and its flux. The spiral galaxy is modeled as an elliptical exponential with six parameters:  $\alpha$  and  $\delta$  of the galaxy center, flux, axis ratio, position angle of the major axis and effective radius. Our model thus has 12 parameters.

In order to obtain the best values we generate images with varying values of these 12 parameters and convolve them with the point spread function as given by bright nearby stars. We then compare the resulting model image with the observed one and compute a  $\chi^2$  goodness of fit. We run a MCMC to obtain the best values for 11 of the 12 parameters. We fix one parameter, the position angle of the major axis, because the large elongation of the galaxy allows a robust direct determination. Table 1 presents the parameters used to constrain the lens model which result from a combination of the parameters found in the three images (*g*, *r*, and *i*). The errors on the fluxes have been artificially increased (see below).

Table 2 gives the measured magnitudes of the two QSO images and the lens galaxy.

TABLE 1  
LENS MODELING CONSTRAINTS OF CY 2201-3201

Parameter	QSO A	QSO B	Galaxy
$\Delta\alpha$ (arcsec)	$0.00 \pm 0.02$	$-0.65 \pm 0.03$	$-0.48 \pm 0.03$
$\Delta\delta$ (arcsec)	$0.00 \pm 0.02$	$-0.51 \pm 0.03$	$0.02 \pm 0.03$
Relative flux	$1.0 \pm 0.2$	$0.9 \pm 0.2$	...
Axis ratio (b/a)	...	...	$0.11 \pm 0.03$
Position angle (degrees) <sup>a</sup>	...	...	140.2
$R_e$ (arcsec)	...	...	$1.4 \pm 0.1$
$V_c(2.7r_o)$ (km s <sup>-1</sup> )	...	...	$130 \pm 20$

<sup>a</sup>Fixed value

### 2.5. Magellan Spectroscopy

On 2004 September 7, 8 and 9, we took spectra of the lens galaxy using the Magellan Clay Boller & Chivens spectrograph (B&C). We use a  $1''$  wide slit aligned along the major axis of the lens galaxy. We use two grisms: 600 and 1200 lines  $\text{mm}^{-1}$ , giving dispersions of 1.6 and 0.8  $\text{\AA}$  pixel<sup>-1</sup>, respectively. We observed the lens for 30 minutes in  $0.8''$  conditions and 3 hr in  $1.2''$  conditions with the lower resolution setting and for 3.5 hrs in  $0.7''$  conditions with the higher resolution set-up. Unfortunately, the slit position moved with respect to the object during the observations and the effective on-source exposure is shorter.

We reduced the images using standard procedures in IRAF. Figure 3 shows the two dimensional low-resolution spectrum at the wavelength of the observed [OII] doublet. We measure the rotational velocity of the disk using the [OII] doublet. We manage to detect signal out to a radius of  $3.8''$  equivalent to 2.7 the effective radius where the rotational velocity appears to have already flattened. In fact for an exponential mass distribution the maximum of the rotational velocity is at approximately twice the effective radius (Binney & Tremaine 1987). In order to obtain a good estimate of the rotational velocity we use an MCMC. We model the two-dimensional spectrum assuming an exponential distribution for the galaxy light and an arc-tangent function for the rotational velocity curve. We generate two-dimensional spectra with the expression

$$I(x, y) = I_o \exp\left(-\frac{y - y_o}{r_o}\right) \frac{2}{\pi} v_c \arctan\left(\frac{x - x_o}{v_o}\right)$$

where  $I_o$  is the normalization,  $y_o$  and  $x_o$  are the pixel coordinates of the center of the galaxy in the two dimensional spectrum,  $r_o$  is the scale radius of the exponential profile,  $v_o$  is the “turnover” rotational velocity radius and  $v_c$  is the asymptotic rotational velocity. We then convolve the model image with a Gaussian of the same width of the seeing in the spatial direction and with a Gaussian of the same width of the spectral resolution in the spectral direction. We generate four model images: one for the low-resolution data taken on September 7, one for the low resolution data taken on September 9, one for the high resolution data taken on September 7 and one for the high resolution data taken on September 8. We compare the model images to the observed ones and compute a global  $\chi^2$  of goodness of fit. We run an MCMC with two free parameters,  $I_o$  and  $v_c$ , to obtain the asymptotic rotational velocity that best fit the

TABLE 2  
MAGNITUDES<sup>a</sup> OF CY 2201-3201

Filter	QSO A	QSO B	Galaxy
<i>g</i>	25.06 <sup>+0.07</sup> <sub>-0.06</sub>	25.22 <sup>+0.11</sup> <sub>-0.10</sub>	22.11 <sup>+0.03</sup> <sub>-0.03</sub>
<i>r</i>	23.09 <sup>+0.05</sup> <sub>-0.05</sub>	23.20 <sup>+0.04</sup> <sub>-0.04</sub>	21.06 <sup>+0.03</sup> <sub>-0.03</sub>
<i>ixs</i>	22.62 <sup>+0.07</sup> <sub>-0.06</sub>	22.74 <sup>+0.03</sup> <sub>-0.03</sub>	20.61 <sup>+0.01</sup> <sub>-0.01</sub>
<i>Ks</i>	18.75 <sup>+0.21</sup> <sub>-0.18</sub>	18.96 <sup>+0.25</sup> <sub>-0.21</sub>	17.18 <sup>+0.29</sup> <sub>-0.23</sub>

<sup>a</sup>Filters *g*, *r*, and *i*: AB system. *Ks*: Vega system

observations. We fix the rest of the parameters ( $y_o$ ,  $x_o$ ,  $r_o$  and  $v_o$ ) to the values directly measured from the two dimensional spectra ( $y_o$  and  $x_o$ ) or the MagIC images ( $r_o$ ). We fix  $v_o$  to the same value in pixels of  $r_o$ . We obtain a best value for the asymptotic rotational velocity of  $V_c = 165 \pm 25 \text{ km s}^{-1}$ . With the arc-tangent rotational velocity model used, we compute a rotational velocity at 2.7 times the scale radius of  $V_c(2.7r_o) = 130 \pm 20 \text{ km s}^{-1}$ . Most of the signal in the fit comes from data interior to this radius and therefore we will use the value at this radius to compare to the lens models that best fit the QSO image positions and fluxes.

In addition we measure the galaxy and QSO redshifts to be  $z = 0.323 \pm 0.001$  and  $z = 3.903 \pm 0.002$ , respectively.

### 2.6. NTT Near-Infrared Imaging

We observed CY2201-3201 with the ESO New Technology Telescope (NTT) on 2004 October 30 in service mode. We took an exposure of 4185 s in the *Ks* band. The reduced combined image provided by ESO had an effective seeing of  $0.75''$ . We calibrated it with standard stars. We use the same MCMC method used for the Magellan images to calculate the positions and fluxes of the three modeled components in this *Ks* image. The calculated positions are much more uncertain than the ones calculated with the Magellan images. The fluxes nevertheless help us constrain the spectral energy distributions of the QSO and lens galaxy (see Table 2).

## 3. LENS MODELING

We model the CY 2201-3201 system using the positions and fluxes of the two QSO images together with the parameters measured for the lens galaxy. We use the GRAVLENS software<sup>11</sup> (Keeton 2001a) developed by C. Keeton. The models used are described in Keeton (2001b). Table 1 summarizes the observational constraints used for the modeling. Note that we have artificially increased the error in the measured fluxes to allow for micro-lensing and/or QSO variability effects. We would like to test the hypothesis that mass is distributed similarly to light, and therefore start modeling the system with one ellipsoidal mass component forced to have the same ellipticity as the one observed in the light. We then add a spherical component meant to represent the galaxy halo, which we then allow to be slightly elongated. We also add external shear to see the role it plays in the overall modeling. In this section we discuss only the constraints enforced by the observed QSO positions and fluxes. We ignore the constraints imposed by

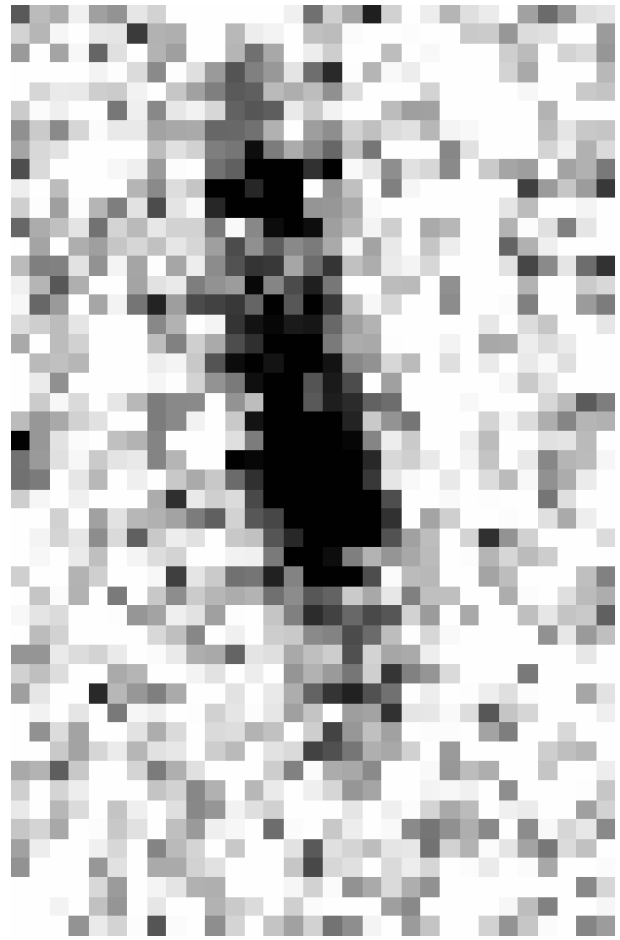


FIG. 3.— Two-dimensional low-resolution B&C Magellan spectrum of CY 2201-3201. The spatial direction runs along the Y-axis and the spectral direction along the X-axis. The sky and galaxy signals have been subtracted.

the third and sometimes fourth images predicted but not seen and the predicted circular velocity of the model. We discuss those constraints in the next section.

### 3.1. One Component Elliptical Mass Models

For simplicity, we start with a singular isothermal ellipsoid (SIE) mass model which gives a flat rotation curve. We follow Keeton (2001b) and use his “alpha” model. The projected mass surface density is given by:  $\kappa(\zeta) = \frac{b'}{2} \zeta^{-1}$ , where  $\zeta = [(1 - \epsilon)x^2 + (1 + \epsilon)y^2]^{1/2}$ .  $\epsilon$  is related to the axis ratio  $q$  by:  $q^2 = \frac{1-\epsilon}{1+\epsilon}$ . We fix the position and ellipticity of the galaxy and only allow the normalization to vary to get the best fit to the observed QSO positions and fluxes. Figure 4 shows the basic configuration of the best fit. Three images of the QSO are produced at one side of the rotation axis of the galaxy. This is a typical spiral galaxy lens configuration (Keeton & Kochanek 1998), with the two brighter images at each side of the disk and the fainter image closer to the disk. Figure 4 shows that the position of the QSO in the source plane (denoted by the plus sign, +) is very close and outside of the radial caustic (*solidellipsoidalline*). If the QSO were closer to the galaxy center and inside this caustic then five images would be produced (with the central one highly demagnified).

Next, we try an elliptical Navarro-Frenk-White (NFW) model (Navarro et al. 1996, 1997). The spherical mass

<sup>11</sup> See <http://www.physics.rutgers.edu/~ckeeton/gravlens/>

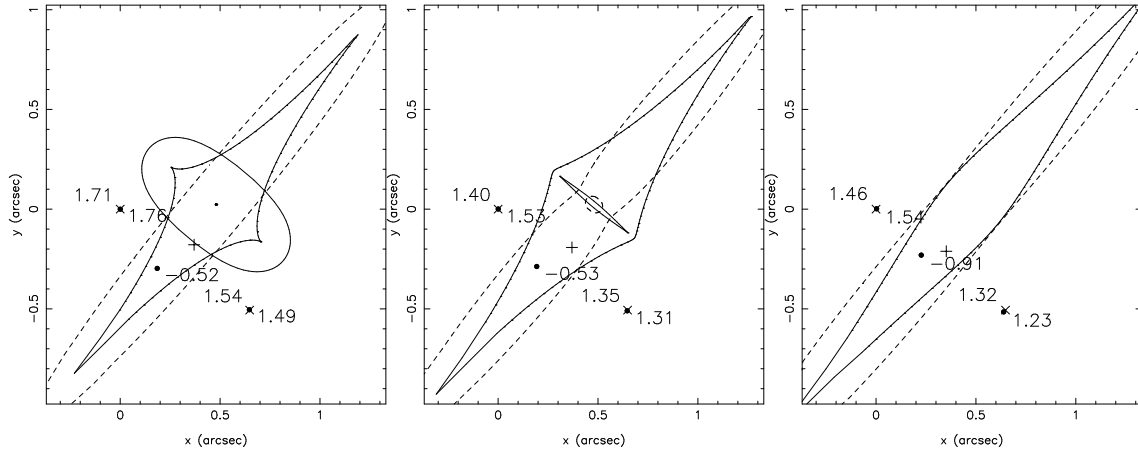


FIG. 4.— Fits to the lens configuration (position and fluxes) for one mass component models. *Left*: SIE model. *Middle*: NFW model. *Right*: Exponential model. The solid lines show the source plane caustics and the dashed lines the lens plane critical curves. The plus sign (+) indicates the position of the QSO in the source plane. The X symbols indicate the two observed positions of the QSO and the dots the predicted positions. The numbers at the right and below of the points give the predicted magnification (positive/negative parity) and the numbers at the left and above the Xs give the re-normalized observed magnifications.

density in the NFW model is given by  $\rho = \frac{\rho_s}{x(1+x)^2}$ , where  $x = r/r_s$ . The projected surface mass density is  $\kappa(r) = 2 \kappa_s \frac{1-F(x)}{x^2-1}$ , where  $F(x)$  is given by equation (48) in Keeton (2001b). See also ?; ?; ?; ?; ?. Keeton’s GRAVLENS code defines an elliptical model from this spherical one replacing the polar radius  $r$  in the projected surface mass density expression by the ellipse coordinate  $\xi = [x^2 + y^2/q^2]^{1/2}$ . This model produces the same “disk” configuration as the previous one. We fit the QSO positions and fluxes allowing only the normalization and characteristic radius of the model ( $r_s$ ) to vary. We find that a large range of values produce acceptable fits. The values of the characteristic radius and normalization that produce acceptable fits are degenerate. The trends in this degeneracy are that, when all other parameters are fixed, the larger the characteristic radius, the lower the normalization and the smaller the radial caustic. That is, the central concentration of the model dictates the size of the radial caustic. Figure 4 shows a typical configuration of this model.

Finally, we model CY2201-3201 with an exponential mass component (Keeton 2001a,b). The projected surface mass density of this model is given by  $\kappa(\xi) = \frac{\kappa_0}{q} \exp(-\xi/R_d)$  where  $\xi$  is the same as above,  $q$  is the axis ratio and  $R_d$  is the scale radius of the exponential distribution. We fix the scale radius, the position angle and the axis ratio to the values obtained with the light distribution (Table 1) and solve for the normalization that best reproduces the position and fluxes. The model shows the disk configuration as before and reproduces the position and fluxes of the two QSO images fairly well (see Fig. 4).

Given that the three models produce acceptable fits, one would like to find another constraint to differentiate between them. Comparing the three models, we find that the position and relative magnification of the third image depend on the concentration of the mass models. For the most concentrated model (SIE), the position of the third image is further away from the galaxy center and the relative magnification compared to the brightest QSO image is the lowest (30%). For the least concentrated model (exponential), the position is closer to the galaxy

center and the relative magnification is the largest (59%).

### 3.2. Two Components Mass Models (Adding a Spherical Halo)

We start with a simple two component model: one SIE, as in the previous section, to which we add a single isothermal sphere (SIS). The SIS model uses the alpha model of Keeton (2001b) (the same as the SIE, see above) in which  $\epsilon = 0$ , the axis ratio  $q = 1$ , and  $\zeta = [x^2 + y^2]^{1/2}$ . We vary the normalizations of the SIS and the SIE models, fixing all other parameters, to find the best fitting model for the observed data. A wide range of normalizations in the models produce acceptable fits to the position and fluxes. All acceptable fits produce five images of the QSO (the central one strongly de-magnified). Only models in which the rotational velocity of the SIS is approximately 50% larger than the rotational velocity of the SIE do not give acceptable fits. Figure 5 shows an example of an acceptable fit in which both components have similar rotational velocities. Best fits are produced for models with larger SIE contribution. In general when the contribution from the spherical component (SIS) gets larger in the fits, then the following trends are observed: the area enclosed by the radial caustic increases and the area enclosed by the tangential caustic decreases; the magnification of the QSO images gets larger and the relative magnification of the fourth brightest image compared to the brightest gets larger. On the other hand, the relative magnification of the third image compared to the brightest is almost independent (staying around 30%) of the ratio of the SIE and SIS contributions. The fourth and fifth images disappear at almost the point where the SIS contribution is negligible and the model is dominated by the SIE component.

We next model the system with an expectedly more realistic mass distribution with two components: an exponential distribution (as in §3.1) to account for the disk and a spherical NFW (same as above but with the axis ratio  $q = 1$ ) representing the halo. We search for models that best fit the data, varying the two normalizations and the characteristic scale  $r_s$  of the NFW model, and fixing all other parameters. Again, acceptable fits to the positions and fluxes are produced for a wide range of model

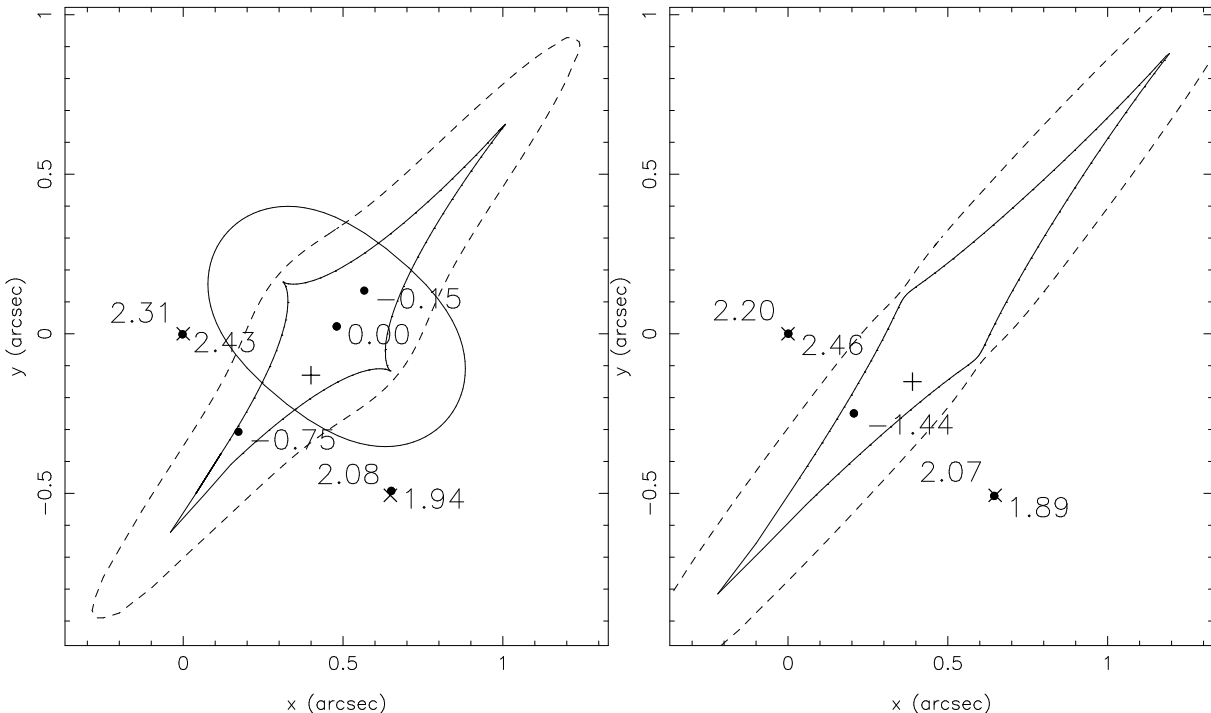


FIG. 5.— Fits to the lens configuration (position and fluxes) for two-mass component models. *Left*: SIE+SIS. *Right*: Exponential+NFW. The symbols are the same as in Fig. 4.

parameters. The only models that are rejected are those in which the spherical NFW component dominates. This occurs when the rotational velocity of the NFW is equal to or 25% larger (depending on the concentration parameter of the NFW) than the rotational velocity of the exponential component at 2.7 disk scale radii. These rejected models produce five images, with the fifth central image strongly demagnified. The only exception is when the combination of the two mass components is such that the QSO needs to be close to the caustic to fit the observed position and fluxes. In this case the fifth image moves away from the center towards the fourth image in the image plane. The trends with respect to the relative strengths of the exponential and NFW components are the following: The larger the NFW spherical component, the worse the fit to the positions and the larger the magnification of the QSO images. The relative magnification of the third brightest image compared to the brightest image goes from  $\sim 50\%$  when the NFW dominates to  $\sim 59\%$  when the exponential dominates.

If we model the halos with some ellipticity, the results present general trends that are between the previous one mass component and two mass components cases discussed. The most significant difference in the case of an exponential plus elliptical NFW model is the magnification of the resulting images. The total magnification of the QSO images is in general lower and the relative magnification of the third image compared to the brightest becomes larger than in the previous cases.

### 3.3. Adding the Rotational Velocity Constraint

In the previous section we restricted ourselves to modeling the system taking into account the positions and fluxes of the two observed QSO images as constraints. We have also measured the rotational velocity of the lens galaxy and can use it as an additional constraint.

For each model we compute the rotational velocity predicted at  $2.7 r_o$ , where  $r_o$  is the scale radius of the exponential distribution of the galaxy light. This is the value of the radius for which we can measure the rotational velocity with our spectroscopic data (see §2.5). All rotational velocity comparisons are performed at this radius, neglecting the rotational velocity dependence with radius.

For the one mass component models, the best fitting SIE model to the QSO image positions and fluxes predicts a lower rotational velocity than observed, but consistent within the  $1 \sigma$  error. The exponential and elliptical NFW models predict larger rotational velocities than observed, which are consistent only at the  $2 \sigma$  level.

If we include the rotational velocity in the overall minimization of the two component models, we find that for the SIE+SIS model the best fit occurs when the rotational velocities of the SIS is approximately 20% lower than the rotational velocity of the SIE. Unacceptable models happen when the rotational velocity of the SIS is  $\sim 5\%$  larger than the rotational velocity of the SIE. For the exponential+NFW case, we do not find acceptable models that satisfy the three constraints: positions and fluxes of the QSO images and rotational velocity of the galaxy. The general trend is that the larger the relative contribution of the spherical component (halo), the lower the rotational velocity predicted to fit the positions and fluxes.

## 4. DISCUSSION

CY 2201-3201 is an edge-on galaxy lens. Such systems offer the possibility of decomposing the relative mass contributions of the disk, bulge and halo. In our optical images CY 2201-3201 appears as a bulgeless edge-on spiral galaxy, producing two images of a background  $z = 3.9$  QSO. We have therefore modeled the system with one (disk) and two (disk+halo) mass components, neglecting

the bulge.

All viable models explored produce either three or four visible images.<sup>12</sup> However, our optical images only show two images of the QSO (Fig 2). We observe the two images that are farther away from the disk but miss the third (and in some configurations the fourth) image located very close to the disk. We have investigated whether dust extinction could be responsible for this missing image. The colors of the QSO images A and B (Table 2) are in fact redder than expected for a typical QSO at that redshift. Although low in signal-to-noise ratio and covering a small wavelength range, the QSO spectrum does not reveal indication of strong intrinsic absorption in the QSO itself. One is then led to conclude that the redder colors are due to dust extinction between the QSO and the observer. The most probable source of attenuation comes from the disk itself. We have computed the amount of dust extinction at the galaxy redshift ( $z = 0.323$ ) necessary to explain the observed colors assuming a mean QSO spectrum at this redshift, no intrinsic absorption at the QSO itself and the value of the local Galactic extinction  $A_V = 0.092$  (Schlegel et al 1998). We find that the QSO image A requires an extinction by the galaxy disk of  $A_V = 1.65$  and the image B an extinction of  $A_V = 1.55$ . Images A and B are seen at a projected distance of  $0.35''$  and  $0.47''$  ( $1.7$  and  $2.2 h_{70}^{-1}$  kpc) of the disk plane respectively. The inferred values of the extinction by the disk are then likely taking into account the projected distances to the disk. Our  $i$  band image is the one with the highest signal-to-noise detection of the QSO images. We have inserted a third image of the QSO in our model images at the position given by our lens models<sup>13</sup> and verify through our MCMC method the maximum flux it could have without being significantly detected. If the ratio of expected flux to maximum observed flux are completely due to absorption by dust at the lens galaxy, then there are at least 3 mag of extinction more at the position of the third image than at the brightest. Taking into account the possible extinction at the brightest image, the third image would suffer  $A_V > 4.7$  of extinction going through the lens galaxy.

In our models of the lens, we have first explored the assumption that the mass distribution has the same ellipticity as the light. We have tried three one-mass component models fixing the galaxy center, axis ratio and position angle to those observed in the optical. We have fit an SIE, an exponential and an NFW model. All three models reproduce the two QSO images and predict a third image that is unobserved. The predicted rotational velocities are consistent with the observed value at the  $1 \sigma$  level for the SIE model and at the  $2 \sigma$  level for the exponential and elliptical NFW models. We have also tried other methods to estimate the galaxy mass. We have fit the observed galaxy photometry with the PEGASE synthesis evolutionary models (Fioc & Rocca-Volmerange 1997). We obtain an absolute magnitude of

$M_r = -20.37 + 5 \log h_{70}$ ,<sup>14</sup> which is a factor 3 fainter than  $L^*$  (Blanton et al. 2003). The stellar mass-to-light ratio ( $M/L$ ) of the best fitting model is  $M/L_V \sim 4.0$ , so its stellar mass would be  $M \sim 3.8 \times 10^{10} h_{70}^{-2} M_\odot$ . The expected rotational velocity for such a mass at 2.7 times the scale radius is  $v_c = 60 - 85 \text{ km s}^{-1}$  (depending on the mass model). The stellar mass by itself is thus insufficient to produce the observed (or predicted) rotational velocity. If we assume the local Tully-Fisher relation (Tully & Fisher 1977; Pierce & Tully 1992; Bell & de Jong 2001; Verheijen 2001) neglecting evolution and the measured absolute magnitude, we obtain a value for the expected rotational velocity of  $v_c \sim 125 - 150 \text{ km s}^{-1}$ , which is consistent with the measured rotational velocity.

We have also studied more realistic models. The galaxy does not appear to have a bulge in the optical images, and therefore we have modelled the system with two mass components: one for the disk and one for the halo. We have tried an SIE+SIS model and an exponential+NFW model. These models reproduce the positions and fluxes of the two observed QSO images. However, the SIE+SIS model predicts four visible images and the best fitting exponential+NFW predicts three visible images. None of these predicted additional images are seen in our images (see above).

We measure a rotational velocity of  $v_c = 130 \pm 20 \text{ km s}^{-1}$  at 2.7 disk scale radius for the lens galaxy. The SIE+SIS model predicts values of the rotational velocity consistent with this value for certain combinations of the relative contributions of the SIE and SIS components (see §3.3). However, the exponential+NFW model predicts higher values of the rotational velocity if we fit the observed position and fluxes of the QSO images. Our Magellan spectroscopic data were obtained on three different nights with two different settings. As explained in §2.5, we have four sets of same night/grating data. The individual fits to the rotational velocity at  $2.7r_o$  for each set of data are  $140 \pm 40$ ,  $160 \pm 45$ ,  $90 \pm 40$ , and  $130 \pm 35$  (low-resolution September 7, low-resolution September 9, high-resolution September 7 and high-resolution September 8, respectively). The relative dispersion of these values may hint at a possible underestimation of the errors. If this were the case, the range of allowed  $v_c$  values would be larger and the exponential+NFW model prediction would still be viable.

We have also explored other effects that can affect our modeling. Our system is likely to be influenced by some external shear which will contribute to the image separation but not to the rotational velocity of the lens galaxy. In fact, CY2201-3201 lies  $7'$  away from the Hickson compact group HCG 90. We have computed what would be the external shear produced by the group assuming it is modeled with a SIE with the same velocity dispersion as measured from the galaxy members. HCG 90 is relatively small and the external shear induced in the CY 2201-3201 system is negligible for our purposes. Apart from HCG 90, CY 2201-3201 appears to be isolated and not in any group, cluster, or obvious large-scale structure. In fact, as part of the CYDER survey we have obtained spectra of several sources in the field and, with the limited spectroscopic data we have, not found any

<sup>12</sup> In fact, there are some possible configurations where the fifth central image, normally largely de-magnified, should also be visible.

<sup>13</sup> Note that the exact position depends on the model. In fact it can be used to distinguish between them. Nevertheless for the purpose used here, the position can be considered similar throughout all plausible models.

<sup>14</sup> Taking into account only the K-correction.  $M_r = -20.11 + 5 \log h_{70}$  adding an evolutionary correction.

sign of a massive structure.

Another possible flaw in our modeling could be that the galaxy center is miscalculated. If the galaxy center is much closer to the QSO images than the position we have measured then most of the discussed configurations would no longer apply and the system would display other image configurations, which can in fact place tighter constraints on the relative contribution of the halo and disk to the total mass budget in the central regions of the lens galaxy. However, the seeing and pixel size of our images and the consistency of the galaxy center in our different filter images make us believe that the true center if different from the one measured should not be very far off.

## 5. CONCLUSIONS

We have presented the discovery and subsequent follow up observations of the CY2201-3201 system composed of an edge-on spiral at  $z = 0.323$  splitting a background  $z = 3.903$  QSO into two observed images each at opposite sides of the disk.

We have modeled the system with one (disk) and two (disk+halo) mass components. The most likely configuration is the “disk” configuration with three images of the QSO one at each side of the disk and the fainter one approximately behind the disk. There are also possible configurations that produce four or even five (this one unlikely) observable images. However we only observe two images. We have discussed the possibility that the third (and fourth, if existent) image is extinguished by the disk. We estimate that an  $A_V > 4.7$  at the predicted position of the third image at the galaxy lens redshift is required to be consistent with our observations.

We have measured the rotational velocity of the lens galaxy to be  $V_c = 130 \pm 20$  km s<sup>-1</sup> at a radius 2.7 times the scale radius of the galaxy exponential light distribution. If we use an SIE+SIS model to fit the QSO image positions and fluxes and this value of the rotational velocity, we find that the contribution by the SIE (disk) to the  $v_c$  at this radius is required to be the same or larger than the contribution of the SIS (halo). If we use an exponen-

tial+NFW model then we are unable to reproduce this value of the rotational velocity if we fit the positions and fluxes of the QSO images. We have speculated whether we have underestimated the error in our determination of the  $v_c$  which would make the exponential+NFW model viable.

CY 2201-3201 is the best lensing spiral galaxy known to date that can be used to disentangle the contributions of its different mass components. Unfortunately our current follow up observations are not constraining enough to elucidate between different possible models. More accurate image source positions, the discovery or not of the predicted third image and the measurement of its properties and a precise rotational velocity would make this system fulfill its potential.

CY 2201-3201 has been awarded *Hubble Space Telescope* (HST) ACS time in cycle 13. We have also been awarded more spectroscopic time at Magellan. We expect that the higher quality images and extra spectra will help us improve our modeling and place strong constraints on the relative contribution of the disk and halo mass components.

We thank C. Keeton for making public his GRAVLENS code and replying to our questions. We thank Paul Schechter for his encouragement and helpful discussions. We thank all observatory staff for their help during observations. We thank the anonymous referee for his/her comments that have helped us improve the paper. F.J.C. acknowledges support from the Spanish Ministerio de Educación y Ciencia (MEC), project AYA2005-09413-C02-01 with EC-FEDER funding and from the research project 2005SGR00728 from the Generalitat de Catalunya. J.M. gratefully acknowledges support from the Chilean Centro de Astrofísica FONDAF 15010003. F.J.C. and J.M. acknowledge support from a “convenio bilateral CSIC-Universidad de Chile”. E.G. is supported by the National Science Foundation under grant AST 02-01667.

## REFERENCES

- Bell, E.F. & de Jong, R.S., 2001, ApJ, 550, 212  
 Binney, J. & Tremaine, S., 1987, Galactic Dynamics (Princeton: Princeton Univ. Press)  
 Blanton, M.R., et al, 2003, ApJ, 592, 819  
 Castander, F.J.; Treister, E.; Maccarone, Th.J.; Coppi, P.S.; Maza, J.; Zepf, S.E. & Guzmán, R., 2003b, AJ, 125, 1689  
 Castander, F.J., Treister, E., Maza, J., Coppi, P.S., Maccarone, T.J., Zepf, S.E., Guzmán, R. & Ruiz, M. T., 2003a, AN, 324, 40  
 Faber, S.M. & Gallagher, J.S., 1979, ARA&A, 17, 135  
 Fiac, M., Rocca-Volmerange, B., 1997, ã, 326, 950  
 Gilks, W.R., Richardson, S. & Spiegelhalter, D.J., 1996, *Markov Chain Monte Carlo in Practice*, Chapman & Hall, London.  
 Hastings, J.K, 1970, Biometrika, 57, 97  
 Huchra, J., Gorenstein, M., Kent, S., Shapiro, I., Smith, G., Horine, E. & Perley, R., 1985, AJ, 90, 691  
 Jackson, N., et al, 1995, MNRAS, 274, L25  
 Keeton, C.R. & Kochanek, C.S., 1998, ApJ, 495, 157  
 Keeton, C.R., 2001a, astro-ph/0102340  
 Keeton, C.R., 2001b, astro-ph/0102341  
 Metropolis, N., Rosenbluth, A.W., Rosenbluth, M.N., Teller, A.H. & Teller, E., 1953, J.Chem.Phys., 21, 1087  
 Navarro, J.F., Frenk, C.S. & White, S.D.M., 1996, ApJ, 462, 563  
 Navarro, J.F., Frenk, C.S. & White, S.D.M., 1997, ApJ, 490, 493  
 Patnaik, A.R., Browne, I.W.A., King, L.J., Muxlow, T.W.B., Walsh, D. & Wilkinson, P.N., 1993, MNRAS, 261, 435  
 Pierce, M.J. & Tully, R.B., 1992, ApJ, 387, 47  
 Pramesh Rao, A. & Subrahmanyam, R., 1988, MNRAS, 231, 229  
 Rubin, V.C. & Ford, W.K., 1970, ApJ, 159, 379  
 Rubin, V.C., Burstein, D., Ford, W.K. & Thonnard, N., 1985, ApJ, 289, 81  
 Schlegel, D.J., Finkbeiner, D.P. & Davis, M., 1998, ApJ, 524, 867  
 Treister, E., Castander, F.J., Maccarone, Th.J.; Gawiser, E., Coppi, P.S., Urry, C.M., Maza, J., Herrera, D., González, V., Montoya, C. & Pineda, P., 2005, ApJ, 621, 104 (T05)  
 Tully, R.B. & Fisher, J.R., 1977, ã, 54, 661  
 Verheijen, M.A.W., 2001, ApJ, 563, 694  
 Winn, J.N., Hewitt, J.N., Patnaik, A.R., Schechter, P.L., Schommer, R.A., López, S., Maza, J. & Wachter, S., 2001, AJ, 121, 1223